Indian Journal of Pure & Applied Physics
Vol. 53, February 2015, pp. 125-133

Dielectric relaxation in double-perovskite Ca_2GdTaO_6

Binita Ghosh[1], Alo Dutta[1], Kumar Brajesh[2] & T P Sinha*[1]

[1]Department of Physics, Bose Institute, Kolkata 700 009, India

[2]University Department of Physics, Veer Kunwar Singh University, Ara 802 301, India

*E-mail: sinha_tp@yahoo.com

Received 26 August 2013; revised 6 May 2014; accepted 20 December 2014

The double perovskite oxide calcium gadolinium tantalate, Ca_2GdTaO_6 (CGT) is synthesized by solid-state reaction technique. The Rietveld refinement of the X-ray diffraction pattern of the sample shows monoclinic phase at room temperature. Fourier transform infrared (FTIR) spectrum shows two primary vibrational modes of the sample at around 378 and 566 cm^{-1}. Dielectric spectroscopy is applied to investigate the *ac* electrical conductivity of CGT in the temperature range 303-673 K and frequency range 42 Hz-1 MHz. The modified Cole-Cole equation is used to describe the relaxation mechanism in CGT. The relaxation time corresponding to dielectric loss is found to obey the Arrhenius law with an activation energy of 0.26 eV. The impedance data has been modeled by an equivalent circuit consisting of two serially connected R-CPE units, one for the grain and the other for the grain boundary, each containing a resistor (R) and a constant phase element (CPE). The frequency dependent conductivity spectra follow the Jonscher power law.

Keywords: Double perovskites, Rietveld grain, Grain boundary, Dielectric properties

1 Introduction

Double-perovskite oxides with general formula $A_2B'B''O_6$, have been attracting much attention in recent years because of their peculiar magnetic and electronic properties due to different cations occupying the octahedral site of the primitive perovskite unit cell. This leads to the strong interaction between electronic, magnetic and structural degrees of freedom that create a great variety of physical and chemical properties of these materials[1]. The complex perovskite system can easily create properties such as superconductivity[2], half metallicity[3], ferromagnetism[4], magnetoresistance[5], magnetodielectric effect[6] etc., depending on the magnetic and electrical characteristics of B' and B" cations.

Takata and Kageyama[7] investigated the microwave dielectric properties of $A(B'_{1/2}B''_{1/2})O_3$-type perovskite ceramics (A = Ba, Sr, Ca; B′ = La, Nd, Sm, Yb and B″ = Nb, Ta) for the first time. Several researchers[8-11] have reported the dielectric properties of a few of such $A(B'_{1/2}B''_{1/2})O_3$-type perovskite ceramics by direct microwave of spectroscopic methods since then. Barium[12], strontium[13] and calcium-based double perovskites[14] with lanthanides were previously studied from the point of view of their MW dielectric properties. Recently,the structural and dielectric properties of Ba_2GdTaO_6 have been investigated[15]. The dielectric properties of the same series by replacing Ba with Ca have been investigated. Investigations of the structure of Ca_2LnTaO_6 [Ln-Lanthamides] using X-ray diffraction experiments reveal that they, generally, possess a monoclinic symmetry[16-18]. Raman spectroscopy of this material Ca_2GdTaO_6 has also been reported[19] in great details, but the dielectric properties of this material are not available in the literature.

In the present paper, the structural and dielectric properties of Ca_2GdTaO_6 (CGT) have been studied. The dielectric and *ac* conductivity properties of CGT have been investigated by alternating current impedance spectroscopy (ACIS) in a wide range of temperature and frequency.

2 Experimental Details

CGT was prepared from $CaCO_3$ (Loba Chemie, reagent grade) and appropriate oxides Gd_2O_3 and Ta_2O_5 (Alfa Aesar, reagent grade) by conventional solid-state synthesis process. Stoichiometric mixtures of the starting powders were homogenized by grinding in acetone medium for 10 h, calcined in an alumina crucible at 1350°C for 20 h and then cooled down to room temperature at the rate of 50°C/h. The powder was then pelletized into disc with the size of 8 mm diameter and about 1.2 mm thickness using polyvinyl alcohol as a binder and then sintered at

1370°C for 10 h and cooled down to room temperature at the rate of 40 °C/h. The crystalline phase and the lattice constants of the sample were determined by powder X-ray diffraction (Rigaku MiniflexII diffractometer) using CuK_α radiation. The data were collected by step scanning over a range of $10° \le 2\theta \le 120°$ in an increment of 0.02°. Rietveld refinement of the diffraction pattern was carried out by the DBWS-9411 Fullprof program[20]. The background was fitted with 6-coefficients polynomial function, while the peak shapes were described by pseudo-Voigt profiles. In all the refinements, scale factor, lattice parameters, positional coordinates and thermal parameters were varied. Occupancy parameters of all the ions were kept fixed during refinement.

The scanning electron micrograph (SEM) of the sample was taken by a FEI Quanta 200 scanning electron microscope. Fourier Transform Infrared (FTIR) spectrum of the sample was recorded between 350 and 4000 cm^{-1} with a Parkin-Elemer FTIR1000 instrument using the KBr pellet technique. The sintered pellet was polished to make both its faces parallel and electroded by high purity ultrafine silver paste for electrical characterization. Capacitance (C), impedance (Z), phase angle (φ) and conductance (G) of the sample were measured both as a function of frequency from 42 Hz to 1 MHz and temperature in the range 303-673 K using a computer controlled LCR-meter (HIOKI-3552). Uncertainty in the measurement of C at low frequency range was about 4%, which decreased to 0.5% at higher frequency range. Uncertainty in the measurement of G at 50 Hz was about 3% and about 0.3% from 10 kHz onwards. The temperature was controlled by Eurotherm 2216e programmable temperature controller connected with the oven. Each measured temperature was kept constant with an accuracy of ±1°C. The real (ε') and imaginary (ε'') components of the complex dielectric constant $\varepsilon^*(=\varepsilon'-i\varepsilon'')$ and the *ac* electrical conductivity $\sigma(\omega) = \omega\varepsilon_0\varepsilon''$ at different temperatures were obtained from the frequency dependence of measured parameters. The value of the active capacitance had been calculated using the formula $C_0 = \varepsilon_0 A/d$ (A is the cross-sectional area and d is plate separation/ thickness of the sample) and found out to be 0.37×10^{-12} Farad.

3 Results and Discussion

3.1 Structural properties (XRD & SEM)

Figure 1 shows the room temperature X-ray diffraction profile of CGT. The continuous curve corresponds to the calculated pattern obtained from Rietveld refinement and the symbols represent the experimental data. The curve at the bottom represents the difference between experimental pattern and the calculated one. Good agreement between the observed and calculated interplaner spacings (d-values) suggests that the compound crystallizes in monoclinic phase with $P2_1/n$ symmetry at room temperature with cell parameters a = 5.5703 Å, b = 5.8389 Å, c = 8.0746 Å and β = 89.737°, which is in excellent agreement with the earlier reported values[16-18]. The structural data obtained from the refinement are given in Table 1. The tolerance factor of the sample is calculated using the formula:

$$T_f = \frac{R_{Ca} + R_O}{\sqrt{2}\left(\frac{R_{Gd} + R_{Ta}}{z} + R_O\right)}$$

where R_{Ca}, R_{Gd}, R_{Ta} and R_O are ionic radii of the respective ions[21]. By geometry, the ideal cubic structure should have T_f = 1, whereas it can be orthorhombic or monoclinic for lower values of T_f. The value of T_f for CGT is found to be 0.88 which significantly deviates from unity giving rise to a distorted structure.

The SEM image of CGT as shown in the inset of Fig. 1, indicates the high density of the material as well as a uniform distribution of grains of different sizes and shapes. The average grain size of CGT is found to be in the range 3-7 μm. The density of the sample has been experimentally found out to be 12.13 g/cm^3 using Archimedes principle whereas the theoretically calculated value is 12.98 g/cc which

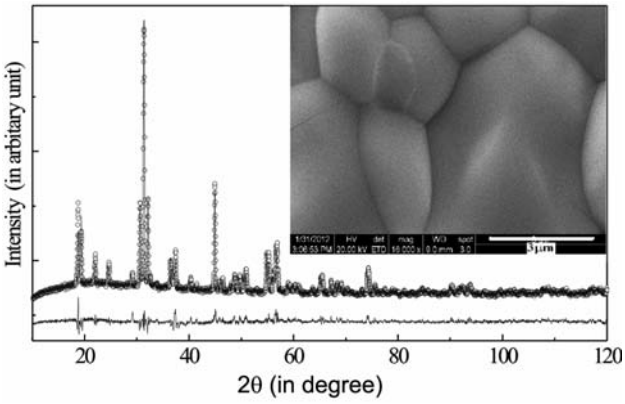

Fig. 1 — Rietveld refinement plot for CGT. The experimental points are represented by symbols and the line represents the simulated XRD data. The scanning electron micrograph of the sample is shown in the inset

Table 1 — XRD fitting and structural parameters

Atom	Site	*x*	*y*	*z*	χ^2	R_p	R_{wp}
Ca	4e	-0.0091	0.5571	0.2437			
Gd	2a	0	0	0			
Ta	2c	0	0	0.5000	2.96	4.85	6.54
O	4e	0.1392(3)	0.0942(6)	-0.2662(6)			
O	4e	0.1583(3)	-0.4806(5)	0.0904(4)			
O	4e	0.1967(9)	0.4717(6)	0.3704(4)			

Bond Length		Bond Angle
$(Gd - O_1) \times 2 = 1.99$ Å	$(Ta - O_1) \times 2 = 2.03$ Å	$<Gd - O_1 - Ta> = 129.42^o$
$(Gd - O_2) \times 2 = 2.34$ Å	$(Ta - O_2) \times 2 = 2.11$ Å	$<Gd - O_2 - Ta> = 101.06^o$
$(Gd - O_3) \times 2 = 3.03$ Å	$(Ta - O_3) \times 2 = 3.14$ Å	$<Gd - O_3 - Ta> = 103.69^o$

shows that the porosity of the material may be approximately 6.5 %.

3.2 FTIR spectroscopy

Figure 2 shows the FTIR spectrum of CGT. All the peaks in Fig. 2 are the characteristics of the material. The spectrum shows three well-defined bands. This is in good agreement with what is systematically found for a perovskite structure in accordance with group theory predictions[22]. The asymmetric stretching and bending modes of the TaO_6 octahedra, usually dominate the IR spectra of perovskite material[23]. Therefore, the energy band at 378 cm^{-1} involves the asymmetric bending mode of the TaO_6 octahedra whilst the other strong broad band at 566 cm^{-1} can be assigned to the asymmetric stretching mode of the TaO_6 octahedra. The same spectral pattern, with two strong and well-defined IR bands in the region 400-650 cm^{-1}, has also been found in a great number of $A_2B'B''O_6$ perovskites[24-28]. Finally, the weak band at 775 cm^{-1} can be assigned to the symmetric stretching mode of the TaO_6 octahedra. This assignment is supported by the fact that in the Raman spectra of different ordered $A_2B'B''O_6$ perovskites[25-27] or perovskite-type materials[22], a strong line related to this mode has been usually observed in the same frequency range. A very small peak at 1635 cm^{-1} comes from the carrier $KBr.(H_2O)_n$.

The logarithmic angular frequency (ω) dependence of the real (ε') and imaginary (ε'') parts of the complex dielectric permittivity (ε^*) of CGT as a function of temperature is shown in Fig. 3(a and b), respectively. The variation of ε' with frequency explains the relaxation phenomenon of the material which is associated with a frequency dependent

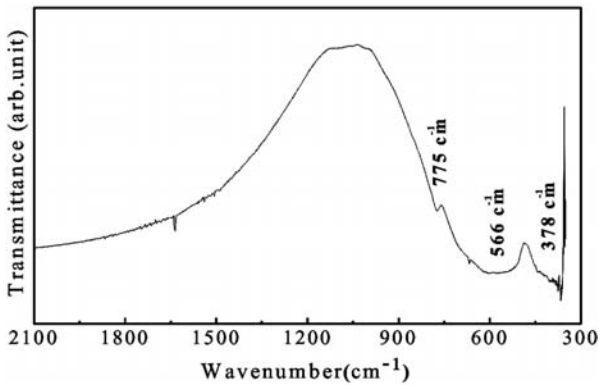

Fig. 2 — FTIR spectrum of Ca_2GdTaO_6

orientational polarization. ε' clearly shows a non Debye-like relaxation having a relaxation peak in ε''. At a particular temperature, if an alternating field is applied then the polarization may fully develop at sufficiently low applied frequencies (the polarization and the field are in phase), but if the frequency of the applied field is too high then the field is reversed before the polarization has responded and no response will be the result of the net effect. The magnitude of the polarization thus drops off beyond a particular frequency. Again at low temperature, the electric dipoles freeze through the relaxation process, and there exists decay in polarization with respect to the applied electric field, which results in the sharp[29] decrease in ε'. When the temperature is high, the rate of polarization formed is quick, and thus the relaxation occurs in high frequency. Qualitatively, this behaviour is observed in Fig. 3(a) and the peak position in ε'' centered at the dispersion region of ε' shifts to higher frequency with the increase in temperature as observed in Fig. 3(b). The high values

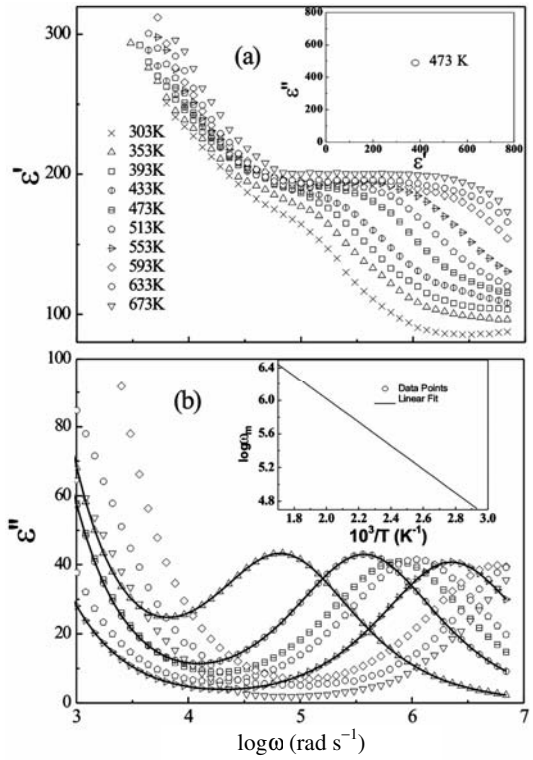

Fig. 3 — Frequency dependences of ε' (a) and ε'' (b) of CGT at various temperatures, where the symbols represent the experimental data points and the solid lines represent the theoretical fitting of ε'' using Eq. (4). A typical Cole-Cole plot is shown in the inset of Fig. 3(a). The Arrhenius plot of ω_m for ε'' is shown in the inset of Fig. 3(b), where the symbols are the experimental points and the solid line is a linear fit to the data points

of ε' at very low frequencies are due to space charge polarization. Normally, space charge (interfacial) polarization occurs when mobile charge carriers are impeded by a physical barrier (i.e. grain boundary) that inhibits charge migration. The charges then pile up at the barrier, producing a localized polarization within grains[30]. The rapid increase in ε'' at low frequencies in Fig. 3(b) indicates the presence of *dc* conductivity σ_{dc} in the material. At low frequencies, *ac* conductivity is similar to *dc* conductivity (σ_{dc} has an observable effect on the loss component of the dielectric response when it is relatively large). With increasing frequency, the effect of *dc* conductivity can be ignored.

In general, the frequency-dependent behaviour of dielectric permittivity can be well described by the simple Cole–Cole relaxation (modified Debye relaxation) equation, which ignores the effect of the electrical conduction[31-33]:

$$\varepsilon^* = \varepsilon_\infty + \frac{\varepsilon_s - \varepsilon_\infty}{1 + (i\omega\tau)^{1-\alpha}} \quad \ldots(1)$$

where ε_s and ε_∞ are the static and high frequency limits of dielectric permittivity, respectively, τ is the most probable relaxation time and α is the Cole–Cole parameter with values between 0 and 1. For an ideal Debye relaxation, $\alpha = 0$. If $\alpha > 0$, it implies that the relaxation has a distribution of relaxation times, leading to a broader peak shape than a Debye peak. However, when the electrical conductivity is dominated at the low frequency range as observed in CGT [Fig. 3(a and b)], a contribution term by electrical conduction is, generally, added to the relaxation equation. The modified Cole-Cole equation that incorporates the conductivity[34,35] term is given by:

$$\varepsilon^* = \varepsilon_\infty + \frac{\varepsilon_s - \varepsilon_\infty}{1 + (i\omega\tau)^{1-\alpha}} - i\frac{\sigma^*}{\varepsilon_0\omega^s} \quad \ldots(2)$$

where $\sigma^* = \sigma_1 + i\sigma_2$ is the complex conductivity. Where σ_1 is the conductivity due to the free charge carrier (*dc* conductivity) and σ_2 is the conductivity due to the space charges (localized charges) and *s* is a dimensionless exponent *(*$0 < s < 1$*)*. For an ideal complex conductivity, $s = 1$. From Eq. (2), the complex permittivity can be decomposed into the real and imaginary parts where:

$$\varepsilon' = \varepsilon_\infty + \frac{(\varepsilon_s - \varepsilon_\infty)\left\{1 + (\omega\tau)^{1-\alpha}\sin\left(\frac{\alpha\pi}{2}\right)\right\}}{1 + 2(\omega\tau)^{1-\alpha}\sin\left(\frac{\alpha\pi}{2}\right) + (\omega\tau)^{2(1-\alpha)}} + \frac{\sigma_2}{\varepsilon_0\omega^s} \quad \ldots(3)$$

and

$$\varepsilon'' = \frac{(\varepsilon_s - \varepsilon_\infty)\left\{1 + (\omega\tau)^{1-\alpha}\cos\left(\frac{\alpha\pi}{2}\right)\right\}}{1 + 2(\omega\tau)^{1-\alpha}\sin\left(\frac{\alpha\pi}{2}\right) + (\omega\tau)^{2(1-\alpha)}} + \frac{\sigma 1}{\varepsilon_0\omega^s} \quad \ldots(4)$$

The first term of Eq. (4) is the part of the losses associated with the dielectric relaxation due to permanent dipole orientation or other motions which do not involve long-range displacement of mobile charge carriers, whereas the second term is the part of the losses associated with long-range migration of

carrier response. From Eqs (3 and 4), the charge carrier localization at defect sites and interfaces (giving σ_2) can make a large contribution to the dielectric permittivity, while the free charge carrier (giving σ_1) contributes to the dielectric loss. Analysis of the experimental data was carried out on the basis of Eq. (4). Typical fitting results are shown in Fig. 3(b) where the solid lines are the fitted curves of experimental results. The excellent agreement between experimental data and calculated data over the entire range of frequencies and temperatures is consistent with Eq. (4) for CGT. It is clearly seen that there are two main factors responsible for the dielectric relaxation of CGT: dipolar[36,37] and conductivity relaxation[38]. The various parameters used in the calculation are listed in Table 2.

In order to elucidate the dielectric relaxation response in CGT, it is important to estimate the activation energy of relaxations. The temperature dependence of the characteristic relaxation time τ_m ($=1/\omega_m$) is shown in the inset of Fig. 3(b), which satisfies the Arrhenius law given by:

$$\omega_m = \omega_0 \exp\left(\frac{-E_a}{K_B T}\right) \quad \ldots(5)$$

where ω_m is the angular frequency corresponding to loss peak value, ω_0 the pre-exponential factor, E_a the activation energy required for dielectric relaxation, T the measuring temperature in kelvin and k_B is the Boltzmann constant. From the numerical fitting analysis, we have obtained the value of the activation energy = 0.264 eV. Such a value of the activation energy indicates that the conduction mechanism for CGT may be due to the polaron hopping based on the electron carriers. In the hopping process, the electron disorders its surroundings by moving its neighbouring atoms from their equilibrium positions, causing structural defects in the *B* sites of the perovskite systems[39].

Figure 4 shows the complex impedance plane plots of CGT at different temperatures. At each temperature, impedance plane plots show two well resolved semicircular arcs, a larger one at lower frequency and a smaller one at the higher frequency side. The appearance of two arcs in the impedance plane plots at each temperature indicates the presence of two types of relaxation phenomena with sufficiently different relaxation times ($\tau = RC$), where R is the resistance and C is the capacitance of the associated phase[40,41]. The complex plane plot is extremely advantageous for distinguishing grain and grain boundary contributions. The size of the semicircular arcs corresponding to grains decreases with the increase in temperature as shown in Fig. 4. The centers of both the semicircular arcs have been found to be depressed below the real axis indicating the heterogeneity and deviation from the ideal behaviour[40]. Since polycrystalline materials,generally, show intergranular or grain-boundary impedances, the impedance data can be best modeled by invoking an equivalent circuit consisting of two serially connected *R-CPE* units, one for the grain and the other for the grain boundary, each containing a resistor (R) and a constant phase element (*CPE*) (instead of ideal capacitor) in parallel[42,43] as shown in the inset of Fig. 4.

An equivalent circuit model (R_gQ_g) ($R_{gb}Q_{gb}$), shown in the inset of Fig. 4 has been employed to interpret the impedance plane plots. Here *R, Q, g* and *gb* are the resistance, the constant phase element, grain elements and grain boundaries, respectively. The CPE is used to accommodate the non-ideal behaviour of the capacitance which may have its origin in the presence of more than one relaxation process with similar relaxation times. The capacitance of the CPE

Table 2 — Fitted values of various parameters for Eq.(4)

Temp (K)	ε_s	ε_∞	α	*s*	ω	σ_1 (Sm^{-1})
393	225	81	0.175	0.80	446680	1.35×10^{-7}
473	250	110	0.175	0.79	957195	2.16×10^{-7}
513	280	130	0.175	0.78	2290868	2.33×10^{-7}
593	310	160	0.175	0.77	5751399	3.92×10^{-7}

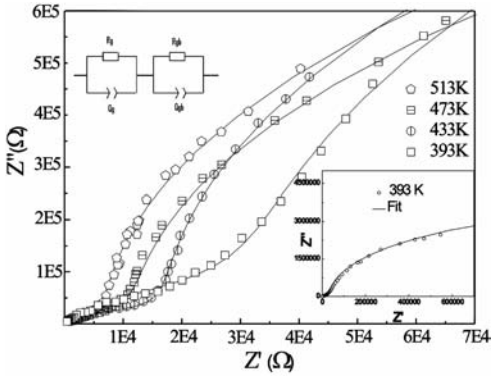

Fig. 4 — Complex impedance plane plots at various temperatures. The corresponding equivalent circuit used to represent the electrical properties of grain and grain-boundary effects is shown in the inset. The entire range of impedance at 393 K temperature is shown in the inset

is given by the following relation $C=Q^{1/n}R^{[(1-n)/n]}$ where the parameter n estimates the non-ideal behaviour having a value of zero for pure resistive behaviour and is unity for capacitative behaviour[44,45]. In these types of perovskites, the grain boundary resistance is,generally, higher in comparison to the grains[46]. Additionally, the arc representing the grain boundaries,generally, lies on the lower frequency side since the relaxation time of the grain boundaries is much larger than that of the grains[43]. Therefore, we assign smaller (high frequency) and larger (low frequency) semicircular arcs to the grains and grain boundaries, respectively[47]. The parameters R_g, R_{gb}, Q_g, Q_{gb}, n_g and n_{gb} were obtained for each temperature by fitting the impedance plane plots. The fitting parameters derived from the equivalent circuit are given in Table 3.

As evidenced from Table 3, the value of n_g increases and n_{gb} decreases with an increase in temperature. These trends signify that the grain capacitance (C_g) is likely to approach ideal behaviour and the grain boundary *(C_{gb})* deviates from the ideal behaviour. A decrease in the capacitance of the grains may be due to the release of trapped charges followed by the accumulation of these charges at the grain boundaries, thereby increasing its capacitance C_{gb}. Table 3 also presents the variations in the resistances of the grain and grain boundaries with temperature. The decrease in the resistance of grains and grain boundaries may be due to the thermal activation of the localized charges. There are two types of thermal activation processes (carrier density in the case of band conduction and carrier mobility in case of hopping), which are responsible for the reduction in the resistive properties with temperature[48]. The grain and grain boundary resistances obey the Arrhenius relation $R=\exp[(E_a/K_BT)]$ where R_0 is the pre-exponential factor, E_a the activation energy, k_B is the Boltzmann's constant. The linear fits shown as straight lines in Fig. 5 yield the values of E_a = 0.2164 and 0.185 eV for the grain and grain boundary, respectively.

Table 3 — Complex impedance plane fitting parameters of Fig. 4 based on the equivalent circuit

Temp. (K)	R_g Ω	R_{gb} Ω	Q_g Ω^{-1} m^{-2} S^{-n}	Q_{gb} Ω^{-1} m^{-2} S^{-n}	n_g	n_{gb}
393	35000	76×10^5	2.25×10^{-8}	9.5×10^{-9}	0.58	0.40
433	18000	56×10^5	1.83×10^{-8}	1.1×10^{-9}	0.61	0.39
473	12800	41×10^5	1.62×10^{-8}	1.0×10^{-9}	0.62	0.38
513	7000	35×10^5	1.21×10^{-8}	0.9×10^{-9}	0.63	0.37

In order to understand the effect of the conductivity on the dielectric properties of CGT, the frequency dependence of *ac* conductivity (σ_{ac}) is further characterized over the temperature range 353-673 K. Fig. 6(a) shows the log-log plot of frequency dependence of real part of *ac* conductivity for CGT at various temperatures.

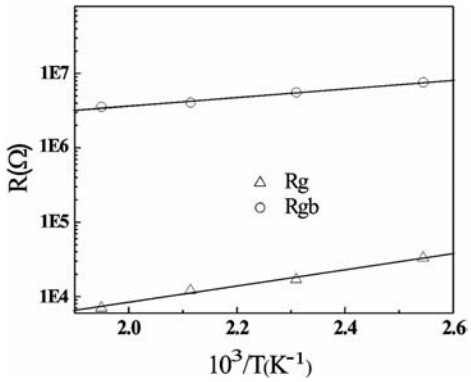

Fig. 5 — Arrhenius plots of the resultant grain and grain boundary resistances. The straight lines are the linear fit to the data points

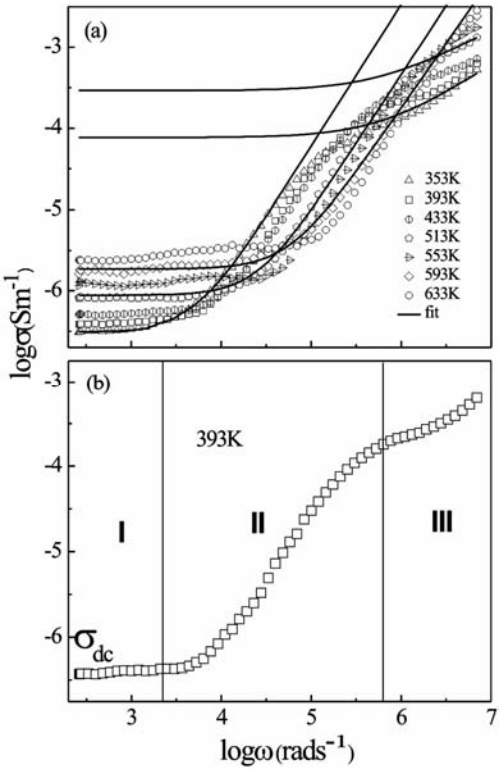

Fig. 6 — (a) Frequency dependence of *ac* conductivity at various temperatures where the symbols represent the experimental data points and the solid lines are the Power law fitting of the same at 353, 513 and 593 K. (b) A typical conductivity spectrum of CGT ceramic at 393 K

Two plateau regions are observed. The low frequency plateau represents the *dc* conductivity (σ_{dc}) whereas the high frequency one represents the contribution of grains to the total conductivity. The presence of both high and low frequency plateaus in the conductivity spectra suggests that the two processes are contributing to the bulk conduction behaviour. The conductivity spectra follow the Jonscher power law[49,50] defined as:

$$\sigma(\omega) = \sigma_{dc}\left[1+\left(\frac{\omega}{\omega_H}\right)^n\right] \quad \ldots(6)$$

where ω_H is the hopping frequency of the charge carriers and n is a dimensionless parameter. The experimental conductivity spectra of CGT are fitted to Eq. (6) for two plateau regions as shown by the solid lines in Fig. 6(a) with σ_{dc} and ω_H as variable and the value of the parameter n is weakly temperature dependent. The value of n varies in the range of $1 \leq n \leq 2$ in the lower frequency region whereas in the high frequency region it is found to be in the range of 0-1. At low frequency, the *ac* conductivity is found to be weakly frequency dependent due to the non-equilibrium occupancy of the trapped charges[45]. As the frequency is further increased, the occupancy of the trap centers is reduced by making them available for conduction. It facilitates the conductive state to become more active by promoting the hopping of electrons and holes. The conductivity increases with increasing frequency and temperature. As shown in Fig. 6(b), a typical conductivity spectrum at 393 K is divided into three parts[51]. In region I, according to the jump relaxation model (since at low frequency and/or at high temperature the electric field cannot perturb the hopping conduction mechanism of charged particles), the conductivity is approximately equal to the *dc* value and the conduction mechanism is the same as that for *dc* conduction, i.e. hopping of charged particles from one localized site to another. The cations surrounded by close packed oxygen anions can be treated as isolated from each other due to direct overlap of the charge clouds. This localization gives rise to the formation of the polaron and the charge transport may be considered between the nearest neighbour sites. The conductivity begins to increase non-linearly after the frequency exceeds the critical frequency ω_c in region II due to the fact that the capacitor admittance becomes numerically larger than the resistor admittance with increasing frequency[52]. In region III, conductivity becomes proportional to frequency, resulting in nearly constant loss (NCL). Thus in CGT it is observed that the NCL regime dominates the *ac* conductivity at high frequency. The activation energy for the thermally activated charge carriers is obtained by fitting the conductivity data using the Arrhenius relation, $\sigma=(\sigma_0/T)\exp[(-E_a/K_BT)]$ where σ_0 is the pre-exponential factor, E_a the activation energy, k_B the Boltzmann's constant. σ is the conductivity in S cm^{-1} given by $\sigma = L/A.R$, where A is area of the sample in cm^2, L is length of the sample in cm, and R (= R_g+ R_{gb}) is the total resistance of the grains and grain boundaries in Ω. The activation energy 0.238 eV has been calculated from the fitted data of the Arrhenius plot as shown in Fig. 7.

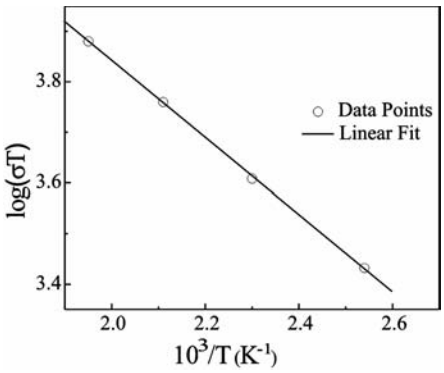

Fig. 7 — Arrhenius plot of the temperature dependence of *dc* conductivity

If we compare the result[15] of CGT with that of Ba_2GdTaO_6 (BGT), it is observed that the conductivity of CGT is less than that of BGT at a particular temperature. This is because when we move from Ba to Ca, the structure changes from cubic with *Fm3m* symmetry to monoclinic with $P2_1/n$ symmetry. Consequently, the value of the tolerance factor T_f decreases from 0.974 to 0.88. Further, the bond lengths B'-O and B"-O and bond angle <B'-O-B"> are found to be different in CGT w.r.t BGT. The bond lengths Gd-O and Ta-O and bond angle <Gd–O–Ta> for BGT is found to be 2.284 Å, 1.994 Å and 180°,respectively[15]. The corresponding values for CGT are listed in Table 1. It is observed that the bond angles <B'-O-B"> for all the three oxygen atoms in CGT are less than that of BGT. Hence, the hybridization between O-*2p* states and Ta-*5d* states arising from electron transfer interaction is weakened

in CGT and may be responsible for the decrease in conductivity of CGT than BGT.

4 Conclusions

The structural characterization of synthesized CGT double perovskite material has been performed with XRD technique. Rietveld analysis reveals that this material crystallizes in a monoclinic perovskite which corresponds to $P2_1/n$ space group. The frequency dependent dielectric dispersion of CGT ceramic has been investigated in the temperature range 303-673 K and in the frequency range f 42 Hz-1 MHz. Grain and grain boundary phases are well resolved by impedance plane plots. The parameters R_g, R_{gb}, Q_g, Q_{gb}, n_g and n_{gb} coupled with the grain and grain boundaries are explained using an equivalent circuit model. Thermal activation of trapped charges/dipoles has been found to be responsible for decreasing the resistance of the grain and grain boundaries and an increase in the value of the dielectric constant and tangent loss. The frequency dependence of the dielectric loss peak is found to obey the Arrhenius law with activation energy of 0.264 eV. The relaxation mechanism of CGT has been discussed in the framework of conductivity and permittivity formalisms.

Acknowledgement

Binita Ghosh acknowledges the financial support provided by the CSIR, New Delhi in the form of RA under grant No. 9/15(0433)/2012 EMR-I. Alo Dutta thanks to Department of Science & Technology of India for providing the financial support through DST Fast Track Project under grant No. SR/FTP/PS-032/2010.

References

1 Hazen R M, *Sci Am*, 258 (1988) 54.
2 Sleight A W, Gillson J L & Bierstedt P E, *Solid State Comm*, 17 (1975) 27.
3 Philipp J B, Majewski P, Alff L, Erb A, Gross R, Graf T, Brandt M S, Simon J, Walther T, Mader W, Topwal D & Sarma D D, *Phys Rev B*, 68 (2003) 144431.
4 Rama N, Philipp J B & Opel M, *J Phys D Appl Phys*, 40 (2007) 1430.
5 Kobayashi K I, Kimura T, Sawada H, Terakura K & Tokura Y *Nature,* 395 (1998) 677.
6 Rogada N S, Li J, Sleight A W & Subramanian M A, *Adv Mater*, 17 (2005) 2225.
7 Takata M & Kageyama K, *J Am Ceram Soc*, 72 (1989) 1955.
8 Zurmuhlen R, Colla E & Dube D C, *J Appl Phys*, 76 (1994) 5864.
9 Zurmuhlen R, Petzelt J, Kamba S, Kozlov G V, Volkov A A & Setter N, *J Appl Phys*, 77 (1995) 5341.
10 Zurmuhlen R, Petzelt J, Kamba S, Kozlov G V, Volkov A A & Setter N, *J Appl Phys*, 77 (1995) 5351.
11 Sreemoolanadhan H, Ratheesh R, Sebastian M T & Mohanan P, *Mater Lett*, 33 (1997) 161.
12 Moreira R L, Khalam L A, Sebastian M T & Dias A, *J Eur Ceram Soc*, 27 (2007) 2803.
13 Khalam L A & Sebastian M T, *J Am Ceram Soc*, 89 (2006) 3689.
14 Khalam L A & Sebastian M T, *J Am Ceram Soc*, 90 (2007) 1467.
15 Ghosh B, Dutta A & Sinha T P, *J of Alloys & Compounds,* 554 (2013) 80.
16 Evdokimov A A, Frolov A M & Vasilev E V, *Inorg Mater,* 20 (1984) 1342.
17 Trunov V K, Konstantinova L I & Evdokimov A A, *Russ J Inorg Chem*, 28 (1983) 807.
18 Filip'ev V S & Fesenko E G, *Sov Phys Crystallogr*, 10 (1965) 243.
19 Dias A, Lage M M, Khalam L A, Sebastian M T & Moreira R L, *Chem Mater*, 23 (2011) 14.
20 Young R A, Sakthivel A, Moss T S & Santos C O P, *Program DBWS*, 941 (1994).
21 Shannon R D, *Acta Crystallogr*, 32 (1976) 751.
22 Licheron M, Gervais F, Coutures J & Choisnet J, *Solid State Commun*, 75 (1990) 759.
23 Ratheesh R, Sreemoolanadhan H & Sebastian M T, *J Solid State Chem*, 131 (1997) 2.
24 Lavat A E, Grasselli M C, Baran E J & Mercader R C, *Mater Lett*, 47 (2001) 194.
25 Corsmit A F, Hoefdraad H E & Blasse G, *J Inorg Nucl Chem*, 34 (1972) 3401.
26 Blasse G & Corsmit A F, *J Solid State Chem*, 6 (1973) 513.
27 Zheng W, Pang W & Meng G, *Mater Lett*, 37 (1998) 276.
28 Dutta A & Sinha T P, *Integrat Ferroelec*, 116 (2010) 41.
29 Lin Y, Jiang L, Zhao R & Nan C W, *Phys Rev B*, 72 (2005) 014103.
30 Hence L L & West J K, *Electronic Ceramics* (Wiley, New York) 1990.
31 Cole K S & Cole R H, *J Chem Phys*, 9 (1941) 342.
32 Macdonald J R, *Impedance Spectros* (Wiley, New York) 2005.
33 Dutta A, Sinha T P & Shannigrahi S, *J Appl Phys*, 104 (2008) 064114.
34 Abdelkafi Z, Abdelmoula N, Khemakhem H, Bidault O & Maglione M, *J Appl Phys*, 100 (2006) 114111.
35 Ming D D, Reau J M, Ravez J, Gitae J & Hagenmuller P, *J Solid State Chem*, 116 (1995) 185.
36 Hippel A R Von, *Dielectric & Waves* (MIT Press, Cambridge) 1954.
37 Park C, *J Korean Phys Soc*, 29 (1996) 327.
38 Macedo P B, Moynihan C T & Bose R, *Phys Chem Glasses*, 13 (1972) 171.
39 Dutta A, Sinha T P & Shannigrahi S, *Phys Rev B*, 76 (2007) 155113.
40 Barsoukov E & Macdonald J R, *Impedance Spectroscopy Theory, Experiments and Applications* (Wiley, New York) 2005.
41 Dhar R, *Indian J of Pure & Appl Phy*, 42 (2004) 56.
42 Sinclair D C & West A R, *J Appl Phys*, 66 (1989) 3850.

43 Macdonald J R, *Impedance Spectroscopy* (Wiley, New York) 1987.
44 Nadeem M, Akhtar M J & Haque M N, *Solid State Commun*, 145 (2008) 263.
45 Nadeem M & Mushtaq A, *J Appl Phys*, 106 (2009) 073713.
46 Ponpandian N,Balaya P & Narayanasamy A, *J Phys Condens Matter*, 14 (2002) 3221.
47 Iguchi E, Nakamura N & Aoki A, *J Phys Chem Solids*, 58 (1997) 755.
48 Idrees M, Nadeem M & Hassan M M, *J Phys D*, 43 (2010) 155401.
49 Jonscher A K, *Dielectric Relaxation in Solids* (Chelsea Dielectrics Press, London) (1983) 161.
50 Hairetdinov E F, Uvarov N F, Patel H K & Martin S W, *Phys Rev B*, 50 (1994) 13259.
51 Li W & Schwartz R W, *Appl Phys Lett*, 89 (2006) 242906.
52 Leon C, Rivera A, Varez A, Sanz J, Santamaria J & Ngai K L, *Phys Rev Lett*, 86 (2001) 1279.